

# Flow instabilities in solar jets in their upstream and downstream regimes

Xiaohong Li, Jun Zhang, Shuhong Yang & Yijun Hou

*CAS Key Laboratory of Solar Activity, National Astronomical Observatories, Chinese Academy of Sciences, Beijing 100101, China;*

lixiaohong@nao.cas.cn; zjun@nao.cas.cn

*School of Astronomy and Space Science, University of Chinese Academy of Sciences, Beijing 100049, China*

## ABSTRACT

Using the Atmospheric Imaging Assembly 304 Å images obtained from the *Solar Dynamics Observatory*, we study two jets which occurred during the M5.8 class flare on 2017 April 3 and the M5.5 class flare on 2016 July 23, respectively. During the M5.8 class flare, many vortex-like structures occurred in the upstream and downstream regimes of the associated jet. While the jet was ejected upwards to the corona, some dark material at its base flowed through a bright structure with a velocity of 110 km s<sup>-1</sup>. The boundary between the material and the structure changed from smooth to uneven. Later, the jet material at the higher atmosphere started to fall down with velocities of over 200 km s<sup>-1</sup>, and the left boundary of the jet developed into a sawtooth pattern. The vortex-like structures were formed, and the growth rates of two structures were presented. During the M5.5 class flare, we also observed many vortex-like structures in the downstream regime of the jet. At the late stage of the jet, some material at the south boundary of the jet fell back to the solar surface, and vortex-like structures at the boundary grew from ripple-like minim into vortices with diameters of 3.4 – 5.4 Mm. The growth rates of the vortex-like structures were calculated. We suggest that the vortex-like structures in the upstream regime are the manifestations of Kelvin–Helmholtz instability, and those in the downstream regime are simultaneously driven by Kelvin–Helmholtz instability and Raleigh–Taylor instability.

*Subject headings:* Sun: activity — Sun: evolution — Sun: filaments, prominences — Sun: flares

## 1. Introduction

Raleigh–Taylor instability (RTI) and Kelvin–Helmholtz instability (KHI) are basic instabilities in fluids and magnetized plasma. The RTI occurs at the interface between two fluids of different densities whenever fluids experience a pressure gradient that opposes the density gradient (Taylor 1950; Sharp 1984). The RTI is mostly gravitationally driven such as a dense fluid is supported against gravity above a lighter fluid. The influence of a magnetic field on the RTI depends on its component parallel to the interface, which can suppress the growth of the magnetic RTI through magnetic tension. Observations of the RTI include mushroom clouds from atmospheric nuclear explosions, supernova explosions in which expanding core gas is accelerated into denser interstellar medium (Wang & Chevalier 2001), and the finger-like structures in Crab Nebula (Hester et al. 1996).

The KHI arises at the interface of two parallel flows. In non-viscous fluids, the KHI will occur as long as there is a velocity shear. Since viscosity and magnetic field have stabilizing influences, a threshold of the velocity difference is required for the KHI to take place in magnetized plasma (Chandrasekhar 1961). In astrophysics and space physics, the KHI has been observed in many active phenomena, e.g., the solar wind (Suess et al. 2009), Earth’s magnetopause (Hasegawa et al. 2004), planetary magnetotails (Masters et al. 2010), and cometary tails (Ershkovich 1980).

Solar atmosphere is made of hot and almost fully ionized plasma. The differences in densities and flow speeds between an expanse of erupting plasma and the background plasma may trigger the RTI and KHI. The RTI in the solar corona has been studied through the formation of plumes when a relatively dense solar prominence overlies a less dense plasma bubble (Ryutova et al. 2010; Berger et al. 2011). The fragmentation of prominence eruption as the material falls back to the solar surface (Innes et al. 2012; Carlyle et al. 2014) and the filamentary structure associated with emerging magnetic flux (Isobe et al. 2005) are manifestations of the RTI as well. These observations are in accordance with the numerical simulations that in three dimensions the RTI results in the formation of finger-like structures elongated in the direction of the magnetic field (Stone & Gardiner 2007). The KHI is also believed to operate in the solar atmosphere, with velocity difference exceeds twice the order of Alfvén velocity. The KHI can be identified by the appearance of growing ripples or the vortices which form across the boundary between two flows. Foullon et al. (2011) observed the KHI in a fast coronal mass ejection (CME) event using the data taken by the *Solar Dynamics Observatory* (*SDO*; Pesnell et al. 2012). Ofman & Thompson (2011) confirmed the occurrence of the KHI in the solar corona, and the KHI in the solar prominence was also investigated by Berger et al. (2010) and Ryutova et al. (2010). Li et al. (2018) reported that the KHI developed at the boundary of a jet due to the strong velocity shear ( $\sim 204$  km

$\text{s}^{-1}$ ) between two flows.

Solar jets, the plasma ejections along the open magnetic field lines in the solar corona, were discovered in the 1980s and then studied after the launch of the Japanese *Yohkoh* satellite in the 1990s (Shibata et al. 1994; Shimojo et al. 1996). Subsequently, the unprecedented high-resolution observations by the *Hinode* (Kosugi et al. 2007), *Solar TERrestrial RELations Observatory (STEREO)* (Kaiser et al. 2008), *SDO*, and *Interface Region Imaging Spectrograph (IRIS)* (De Pontieu et al. 2014) have made great improvements in our understanding of the solar jets (Savcheva et al. 2007; Shen et al. 2011; Tian et al. 2014). Solar jets have been observed all over the solar atmosphere including coronal holes (Yang et al. 2011b), quiet regions (Hong et al. 2011) and active regions (Li et al. 2015). Many wavelengths, e.g., X-ray (Sterling et al. 2015), extreme ultraviolet (EUV; Chae et al. 1999) and  $\text{H}\alpha$  (Yokoyama & Shibata 1995) are employed to detect the jets. Coronal jets have apparent lengths of 10 – 400 Mm and widths of 5 – 100 Mm. The speeds of jets range from 10 to 1000  $\text{km s}^{-1}$ , with a mean value of 200  $\text{km s}^{-1}$  (Shimojo et al. 1996). The lifetimes of jets are 10 – 70 min, with a median value of 20 – 40 min (Nisticò et al. 2009). Jets have temperature in the range of 0.05 to 2.0 MK, while electron densities have been reported as  $6.6 \times 10^9$  to  $3.4 \times 10^{10} \text{ cm}^{-3}$  (Yang et al. 2011a). The magnetic field strength of the jets is a few Gauss (Pucci et al. 2013). The morphology, formation mechanisms and dynamic characters of the jets, as well as their relations to other coronal structures, have been carefully studied (Raouafi et al. 2016). However, studies of the instabilities in solar jets are still in early stages.

In this study, using the high-resolution data from the *SDO*, we present observations of the vortex-like structures in two solar jets. The first jet was located at active region (AR) 12644 and was associated with an M5.8 class flare on 2017 April 3. During this jet, we observed the vortex-like structures both in its upstream and downstream regimes, i.e., when the jet was ejected upwards to the corona and fell down from the higher atmosphere. We also observed the vortex-like structures driven by the falling material of the jet during the M5.5 class flare on 2016 July 23. The vortex-like structures in the upstream regime of the jet are interpreted as evidence of the KHI, and the vortex-like structures in the downstream regime may be caused by both the RTI and KHI.

## 2. Observations and data analysis

We adopted the Atmospheric Imaging Assembly (AIA; Lemen et al. 2012) multi-wavelength images and the Helioseismic and Magnetic Imager (HMI; Scherrer et al. 2012; Schou et al. 2012) data on board the *SDO*. For the M5.8 class flare on 2017 April 3, we chose the AIA

304 Å images, obtained from 14:00 UT to 16:00 UT with a pixel size of  $0''.6$  and a cadence of 12 s. We also used the intensitygram from the HMI, with a spatial sampling of  $0''.5 \text{ pixel}^{-1}$  and a 15 min cadence, i.e., one frame in twenty, from 2017 April 3 00:00 UT to 2017 April 4 00:00 UT. For the M5.5 class flare on 2016 July 23, we employed the AIA 304 Å images from 05:30 UT to 06:30 UT with a pixel size of  $0''.6$  and a cadence of 12 s. In addition, we also employed the *Geostationary Operational Environmental Satellite (GOES)* data with the 1 min cadence to examine the variation of soft X-ray 1–8 Å flux.

### 3. Results

On 3 April 2017, there were five ARs on the solar disk, and AR 12644 we focus on was located at the west boundary. At 14:19 UT, an M5.8 class flare took place in this AR. Associated with the M5.8 class flare, a jet occurred on the north side and its brief evolution is shown in Figure 1. The HMI intensitygram in panel (a) shows the location and appearance of the sunspot of AR 12644. The *GOES* soft X-ray 1–8 Å flux (see green curve in panel (b)) shows that the M5.8 class flare reached its peak at 14:29 UT, and the appearances of the flare and the jet at this moment are shown in panel (b). The jet took place at about 14:20 UT, and we observed numerous vortex-like structures during its evolution. The green rectangle in panel (c) and square in panel (d) display the positions where the vortex-like structures are observed, respectively.

Figure 2 shows the development of vortex-like structures which happened near the base of the jet. At 14:30 UT, the main mass of the jet was ejected outwards. At the base of the jet, some dark material flowed through the bright structure with a velocity of  $110 \text{ km s}^{-1}$ , and the boundary between the material and the structure was smooth as shown in panel (a). Then, the boundary became distorted as denoted by the blue curves in panels (b)–(d). The biggest distortion in each panel is indicated by the blue arrow, with a size scale of  $1.7 - 2.5 \text{ Mm}$ . The green arrows in panel (e) denote several vortex-like structures, and the distance between two nearby structures is roughly  $2.7 - 3.8 \text{ Mm}$ . The vortex-like structures such as knots, growing ripples and so on are common phenomena in the solar atmosphere (Severny & Khokhlova 1953; Rothschild et al. 1955; Sakurai 1976; Ofman & Thompson 2011). Some researchers interpreted the vortex-like structures appearing on the boundary between the jet and the ambient background as evidence of the KHI (Li et al. 2018; Zhelyazkov & Chandra 2018). Here, the velocity shear between the dark material and the bright structure drove the KHI, and the vortex-like structures were formed consequently. As the KHI developed, these structures became turbulent (see panels (f) and (g)). After the KHI, the boundary began smooth again as shown in panel (h).

Figure 3 and Movie1 show the evolution of the vortex-like structures at the left boundary of the jet. Due to the gravity, the jet material whose speed didn't reach the escape speed started to drop at about 15:14 UT from the higher atmospheric layer. Along the left boundary of the jet (see slice “A–B” in panel (f)), we made a slice and the space-time plot is displayed in panel (h). We chose some trajectories and determined that the falling velocities of the jet material were approximately  $224 - 289 \text{ km s}^{-1}$ . The left boundary of the jet was smooth initially, as shown in panel (a). At about 15:25 UT (see panel (b)), the boundary began to display ripple structures. These structures gradually developed and grew up into vortex-like structures which are displayed in panels (c) and (d). We chose some significant structures (see the green rectangle in panel (e)) when they were biggest and enlarged these structures in panel (g). The deformations were roughly  $6.4 - 8.8 \text{ Mm}$ . We chose two structures in panel (g) and measured their deformations over time. The deformations in three minutes are plotted in Figure 4. The deformations were exponential growths  $d = d_0 e^{\gamma t}$ , and the growth rates  $\gamma$  were estimated to be 0.0097 and 0.0088.

As the falling jet material was denser than the surrounding corona, and the interface was at some angle to gravity (the green arrows in Figure 3(b) display the directions of gravity at the points where the arrows start), these vortex-like structures in the downstream regime of the jet may be caused by the RTI. When magnetic field is not involved, the growth rate of the RTI is give as (e.g., Chandrasekhar 1961; Ryutova et al. 2010)

$$\gamma = \sqrt{(\rho_u - \rho_l)gk/(\rho_u + \rho_l)} \quad (1)$$

where  $k$  is the wavenumber,  $g$  is the acceleration due to gravity,  $\rho_u$  is the upper density and  $\rho_l$  is the lower density (relative to the direction of gravity). We take the electron number density of the surrounding environment to be equal to  $n_l = 10^{15} \text{ m}^{-3}$ , and the electron number density of the jet is  $n_u = 10^{16} \text{ m}^{-3}$ , then the density can be derived as  $\rho = n \cdot m$  ( $m = 1.673 \times 10^{-27} \text{ kg}$ ). The solar gravitational acceleration is  $273.2 \text{ m s}^{-2}$ , then  $g$  is  $236.6 \text{ m s}^{-2}$  considering the angle between the gravity and the interface as 60 degrees. The distance between two structures is regarded as the characteristic wavelength ( $\sim 5000 \text{ km}$ ). Thus, we can estimate that the growth rate is 0.0156 when the RTI is pure gravitationally driven. In solar jets, the magnetic field constrains the motion of the plasma. The inclusion of magnetic field adds a criterion for the occurrence of the RTI (Chandrasekhar 1961; Sharp 1984):

$$kg(\rho_u - \rho_l)/(\rho_u + \rho_l) > [(k \cdot \vec{B}_u)^2 + (k \cdot \vec{B}_l)^2]/\mu_0(\rho_u + \rho_l) \quad (2)$$

where  $\vec{B}_u$  and  $\vec{B}_l$  are the magnetic intensity of the upper and lower regions, respectively. Chen et al. (2012) assumed that the magnetic flux across the transverse section of the jet would remain constant and found that the magnetic field inside the jet gradually decreases with the height from  $15 \pm 4 \text{ G}$  to about  $3 \pm 1 \text{ G}$  at a height of  $7 \times 10^4 \text{ km}$  ( $\sim 100''$ ). Here,

the heights where the vortex-like structures occurred were more than 100'', so we assumed the magnetic field parallel to the interface to be  $B_u = B_l = 3$  G. In consequence, the left term in equation (2) is approximately  $2.43 \times 10^{-4}$ , and the right term is  $1.23 \times 10^{-2}$ , under which condition the RTI won't happen. As seen from the formula, the occurrence of the RTI would be influenced by the density and the magnetic field intensity. When the density of the jet  $\rho_u$  increases 10 times, the first term changes a little while the second term becomes approximately one-tenth of what it is now. So in a magnetohydrodynamic environment like corona, the RTI would happen when the density is high enough ( $n > 10^{18} \text{ m}^{-3}$ ), that's the reason why so far very few case of filament eruption observed the RTI. When the magnetic field intensity becomes  $B_u = B_l = 2$  G, the right term would change to four-ninths of the previous value ( $\sim 5.5 \times 10^{-3}$ ). The density contrast of solar jets relative to background is not adequate for the RTI to develop, so other reasons may also contribute to the formation of the vortex-like structures. In our case, as there were velocity differences ( $224 - 289 \text{ km s}^{-1}$ ) between the dropping jet material and the ambient corona, the occurrence of the vortex-like structures may be driven by the KHI as well. When the gravity (the RTI) is not considered, the onset condition of the pure KHI in magnetized incompressible ideal plasma can be deduced by (Chandrasekhar 1961; Cowling 1976)

$$(\vec{k} \cdot \vec{V}_u - \vec{k} \cdot \vec{V}_l)^2 > (\rho_u + \rho_l)[(\vec{k} \cdot \vec{B}_u)^2 + (\vec{k} \cdot \vec{B}_l)^2]/\mu_0\rho_u\rho_l \quad (3)$$

where  $\vec{k}$ ,  $\vec{V}$ ,  $\vec{B}$ ,  $\rho$  are the wave vector, velocity, magnetic field intensity and mass density in the flux tube, respectively. The subscripts 'u' ('l') indicate the quantities of the upper (lower) region. Presuming that  $\vec{k} \parallel \vec{V}_u \parallel \vec{V}_l \parallel \vec{B}_u \parallel \vec{B}_l$ , then the velocity difference threshold is

$$\Delta V_s = |\vec{V}_u - \vec{V}_l| = \sqrt{(\rho_u + \rho_l)(B_u^2 + B_l^2)/\mu_0\rho_u\rho_l}. \quad (4)$$

Substituting the values into the formula, we can estimate that the velocity difference threshold is  $307 \text{ km s}^{-1}$ . When the magnetic field intensity decreases to  $B_u = B_l = 2$  G, the velocity difference threshold decreases to  $205 \text{ km s}^{-1}$  accordingly, and the KHI would happen. When the gravity is included, the instability would happen if (Chandrasekhar 1961)

$$\Delta V > \sqrt{(\rho_u + \rho_l)(B_u^2 + B_l^2)/\mu_0\rho_u\rho_l - (\rho_u + \rho_l)(\rho_u - \rho_l)g/k\rho_u\rho_l}. \quad (5)$$

If  $\rho_u < \rho_l$ , the second term beneath the radical sign will largen the velocity difference threshold, which means that the gravity with density gradient suppresses the KHI. If  $\rho_u > \rho_l$ , the second term will diminish the velocity difference threshold, which can be regarded as the manifestation of the RTI. Under our previous assumptions, the velocity difference threshold declines slightly ( $304 \text{ km s}^{-1}$  when  $B_u = B_l = 3$  G and  $201 \text{ km s}^{-1}$  when  $B_u = B_l = 2$  G), and the second term below the radical sign is roughly one-fiftieth of the first term, implying

that the influence of the gravity may be very small. As the practical situation is complex, it is difficult to decide which instability is dominant. Hence, we interpret the occurrence of vortex-like structures as the result of both the RTI and the KHI. Under this circumstance, the growth rate (the imaginary part of frequency) can be deduced by (Guglielmi et al. 2010; Berger et al. 2017)

$$\gamma = \sqrt{k g (\rho_u - \rho_l) / (\rho_u + \rho_l) - k^2 (B_u^2 + B_l^2) / \mu_0 (\rho_u + \rho_l) + k^2 \rho_u \rho_l (\Delta V)^2 / (\rho_u + \rho_l)^2}. \quad (6)$$

The growth rate is sensitive to changes in magnetic field intensity. Choosing  $\Delta V = 250$  km s<sup>-1</sup>, when  $B_u = B_l = 3$  G, the instability won't take place. When  $B_u = B_l = 2$  G, the growth rate is roughly 0.054, much higher than we estimated. Using the measured growth rate ( $\sim 0.009$ ), we can estimate that the magnetic field intensity is approximately 2.5 G ( $B_u = B_l$ ), which is consistent with the actual magnetic field intensity of the jet and the corona (Chen et al. 2012).

We also observed the vortex-like structures caused by falling material in another jet which occurred on July 23, 2016. This jet took place in AR 12565 which was located on the west side of the solar disk. At 05:27 UT, an M5.5 class flare occurred, accompanying a large scale jet (see Figure 5(a)). Massive plasma was ejected outwards. Later, some plasma fell back to the solar surface, and vortex-like structures developed at the south boundary of the jet as shown in panels (b1)–(b5) and Movie2. The south boundary of the jet was smooth at first (see panel (b1)). At 05:48 UT, the boundary started to have ripple structures, which are indicated by the cyan arrows in panel (b2). The average distance between two adjacent structures was roughly 10 Mm. We studied the plasma movement at the positions of slices “A–B” and “C–D” (see panel (b4)), and the temporal evolutions are displayed in Figures 6(a) and (b), respectively. At around 05:48 UT (see the vertical dashed lines in Figures 6(a) and (b)), the plasma at the south boundary of the jet started to fall back from the higher solar atmospheric layer. We chose several representative structures and measured their velocities, with values from 110 km s<sup>-1</sup> to more than 270 km s<sup>-1</sup>. Same as the last jet example, the gravity opposed the density gradient of the jet and the ambient corona, and was at some angle to their interface (see the green arrows in Figure 5(b2) which display the directions of gravity at the start points). Also, there existed velocity shear between the falling material and the ambient corona, so the vortex-like structures began to grow at the south boundary driven by both the RTI and the KHI. We chose three isolated structures (indicated by arrow “1” in Figure 5(b3) and arrows “2” and “3” in Figure 5(b5)), and their evolutions are presented in Figure 7.

Figure 7(a) is the space-time stack plot along the green enclosed area in Figure 5(b3) from 05:50 UT to 05:52 UT. The cadence of AIA 304 Å data is 12 s, so there are ten images in two minutes. The blue arrows denote a vortex-like structure (indicated by arrow “1” in

Figure 5(b3)), and its morphological changes and position movements are displayed. In the first image of panel (a), structure “1” looks like a ripple. Along with the development of the KHI over time, the structure grew and became a vortex-like structure. The diameter of structure “1”, marked by the cyan lines and arrows, is about 4.2 Mm in the last image of panel (a). Using the method displayed in Figure 4, we measured the changes of the vortex size (diameter) over time and determined the growth rate  $\gamma$  to be roughly 0.0087. Along the boundary of the jet, structure “1” moved approximately 21.8 Mm ( $\sim 30''$ ) in two minutes, thus the velocity of structure “1” was about  $181 \text{ km s}^{-1}$ . Figure 7(b) is the space-time stack plot along the green enclosed area in Figure 5(b3) from 06:02 UT to 06:06 UT with a cadence of 24 s. The white arrows indicate the vortex-like structure pointed by arrow “2” in Figure 5(b5). In 168 s, structure “2” developed to a vortex-like structure with a diameter of 3.4 Mm (the cyan lines and arrows in the seventh image) and moved 21.0 Mm ( $\sim 29''$ ), with the velocity of  $125 \text{ km s}^{-1}$ . The growth rate of structure “2” was estimated to be about 0.0070. There is another structure indicated by the green arrows in Figure 7(b) and arrow “3” in Figure 5(b5). This structure was tiny at first and grew to a clear vortex in the end, with the diameter of 5.4 Mm (see the cyan lines and arrows in the last image). The growth rate of structure “3” was approximately 0.0068. The position of structure “3” changed 32.6 Mm ( $\sim 45''$ ) in four minutes, and the velocity of this structure was roughly  $136 \text{ km s}^{-1}$ . As demonstrated before, the growth rate can be estimated using equation (6) when both the RTI and KHI are considered. Here, we use the same assumption that  $B_u = B_l = 2 \text{ G}$ ,  $n_u = 10^{16} \text{ m}^{-3}$  and  $n_l = 10^{15} \text{ m}^{-3}$ . The distance between two adjacent structures ( $\sim 10 \text{ Mm}$ ) was regarded as wavelength. Considering the angle between the gravity and the interface as 45 degrees and the velocity difference as  $\Delta V = 200 \text{ km s}^{-1}$ , then the growth rate is estimated to be 0.0057. Remarkably, the measured values (0.0068 – 0.0087) are of the same order of the theoretically estimated values, implying that these vortex-like structures are simultaneously driven by the KHI and RTI.

#### 4. Conclusions and Discussion

With the *SDO* observations, we studied the M5.8 class flare and the associated jet in AR 12644. There occurred many vortex-like structures during the development of the jet. As the jet material was ejected to the corona, dark material flowed through the bright structure at the base of the jet with velocity of  $110 \text{ km s}^{-1}$ , causing the KHI. The boundary between dark material and bright structure became distorted, and vortex-like structures grew with the biggest distortion of 1.7 – 2.5 Mm. Due to the gravity, the jet material whose speed didn’t reach the escape speed dropped down from the high atmospheric layer. The jet was denser and over  $200 \text{ km s}^{-1}$  faster than the ambient corona, thus the RTI and KHI occurred,



and the boundary which was smooth at first started to display vortex-like structures with distortions of 6.4 – 8.8 Mm. We also studied the M5.5 class flare on 2016 July 23, and at the south boundary of the concomitant jet, the vortex-like structures also generated because of falling material. The south boundary was smooth initially. Due to the density difference and velocity shear ( $\sim 110 \text{ km s}^{-1}$  to more than  $200 \text{ km s}^{-1}$ ) between the jet and the background, the RTI and KHI took place, and the boundary became distorted. We analysed the evolution of the boundary, and there were small structures grew from ripple-like minim into vortices whose diameters were roughly 3.4 – 5.4 Mm. The growth rates of the structures were approximately 0.0068 – 0.0087, and the downward velocities of these structures were over  $100 \text{ km s}^{-1}$ .

In the upstream regime of the jet, the vortex-like structures such as blobs appearing on the boundary between the jet and the corona have been reported before (Li et al. 2018; Zhelyazkov & Chandra 2018; Bogdanova et al. 2018), and they are interpreted as evidence of the KHI. The theory of the KHI in solar jets has been developed in recent years, and Magnetohydrodynamic (MHD) simulations support the presence of the KHI in solar jet (Zaqarashvili et al. 2015; Kuridze et al. 2016). Considering the distance between two structures (2.7 – 3.8 Mm) as wavelength ( $\sim 3000 \text{ km}$ ), substituting the value  $B_u = B_l = 3 \text{ G}$ ,  $n_u = 10^{16} \text{ m}^{-3}$  and  $n_l = 10^{15} \text{ m}^{-3}$  into equation (5), we can estimate that the velocity difference threshold of the KHI when the jet was ejected upwards was roughly  $309 \text{ km s}^{-1}$ , a little larger than the value when the gravity is not involved ( $307 \text{ km s}^{-1}$ ). Here, the KHI occurred when the velocity difference was  $110 \text{ km s}^{-1}$ , and there may be many reasons. First of all, the density of the bright structure may be larger than that of the corona. If we change the density of the bright structure to be  $n_l = 10^{16} \text{ m}^{-3}$ , then the velocity threshold becomes  $131 \text{ km s}^{-1}$  accordingly. From the results, we can see that density contrast has a huge impact on the onset of the KHI. What's more, the estimation is established under many preconditions, e.g., the plasma is incompressible, ideal and  $\vec{k} \parallel \vec{V}_u \parallel \vec{V}_l \parallel \vec{B}_u \parallel \vec{B}_l$ , thus many parameters can influence the occurrence of the KHI besides the velocity and density contrast. As seen from equation (3), the effect of a magnetic field on the KHI depends on both its intensity and orientation. Only magnetic field component parallels to the interface discontinuity can exert a restoring force and suppresses the growth of the KHI, thus the magnetic field configurations of the jet and surrounding environment may affect the occurrence of KHI. Zhelyazkov et al. (2015) investigated the KHI in surges (cool jets) by modelling the surge as a moving twisted magnetic flux tube in homologous and twisted magnetic field. Their numerical studies showed that KHI occurred in both magnetic field configurations for MHD waves propagating in axial direction, and the critical velocity for emerging KHI was remarkably lower ( $24 - 60 \text{ km s}^{-1}$ ) when both magnetic field was twisted. Also, the compressibility of the plasma may change the instability criteria and growth rates (Sen 1964). Regarding

EUV jets as a vertically moving flux tube (untwisted and weakly twisted), Zhelyazkov et al. (2016) found that the critical jet velocity was  $112 \text{ km s}^{-1}$  when jet was assumed to be compressible plasma, and when the jet and its environment were treated as incompressible, the critical velocity became  $114.8 \text{ km s}^{-1}$ . Their work also proved that a weak twist of the magnetic field in the same approximation may decrease the threshold. What's more, viscosity may have a destabilizing influence when the viscosity coefficient takes different values at the two sides of the discontinuity, and therefore decrease the criteria of KHI (Ruderman et al. 1996). All these results reveal that the criteria of KHI can be reduced by many factors, and KHI can happen under the velocity difference of  $110 \text{ km s}^{-1}$  in the upstream regime of the jet.

Here, we also report the vortex-like structures occurred when the jet material fell down, and these structures are interpreted as the result of the KHI and RTI. The coexistence of the RTI and KHI is not rare. In the nonlinear evolution of the RTI, the secondary KHI can be triggered as a result of the shear flows that develop between the falling material and the background (Cattaneo & Hughes 1988). Similarly, in the nonlinear evolution of the KHI, the rolled-up KH vortices would generate centrifugal force and create the conditions for the development of the RTI. In a more general case, there exist both the RTI and the KHI at the very beginning of a real system (Ye et al. 2011; Hillier 2018). In the downstream regime of the jet, the density and velocity differences between the jet material and the corona may trigger the RTI and KHI, as long as the stabilizing effect of the magnetic field are surpassed. Through theoretical analysis, the coaction of the RTI and the KHI in solar jet are proved, and there is little difference between the observed growth rates with the theoretical ones. The combination of the RTI and KHI has been studied before theoretically and observationally, which is so-called coupled KH-RT instability or combined RT-KH instability (Farrugia et al. 1998; Berger et al. 2017). As we demonstrated before, there exist many preconditions in the derivation, and the occurrence of the KHI can be influenced by many factors. These factors such as the twisting of the magnetic field, the compressibility and viscosity of the fluids, and ion-neutral collisions would influence the RTI as well (Stone & Gardiner 2007; Liberatore et al. 2009; Díaz et al. 2012; Hillier 2016).

We thank the referee for valuable suggestions. This work is supported by the National Natural Science Foundations of China (11533008, 11790304, 11673035, 11773039, 11673034, 11790300), Key Programs of the Chinese Academy of Sciences (QYZDJ-SSW-SLH050), and the Youth Innovation Promotion Association of CAS (2014043). The data are used courtesy of HMI, AIA and *GOES* science teams.

## REFERENCES

- Berger, T., Hillier, A., & Liu, W. 2017, *ApJ*, 850, 60
- Berger, T., Slater, G., Hurlburt, N., et al. 2010, *ApJ*, 716, 1288
- Berger, T., Testa, P., Hillier, A., et al. 2011, *Nature*, 472, 197
- Bogdanova, M., Zhelyazkov, I., Joshi, R., & Chandra, R. 2018, *New A*, 63, 75
- Carlyle, J., Williams, D. R., van Driel-Gesztelyi, L., et al. 2014, *ApJ*, 782, 87
- Cattaneo, F., & Hughes, D. W. 1988, *Journal of Fluid Mechanics*, 196, 323
- Chae, J., Qiu, J., Wang, H., & Goode, P. R. 1999, *ApJ*, 513, L75
- Chandrasekhar, S. 1961, *International Series of Monographs on Physics*, Oxford: Clarendon, 1961,
- Chen, H.-D., Zhang, J., & Ma, S.-L. 2012, *Research in Astronomy and Astrophysics*, 12, 573
- Cowling, T. G. 1976, *Monographs on Astronomical Subjects*, Bristol: Adam Hilger, 1976,
- De Pontieu, B., Title, A. M., Lemen, J. R., et al. 2014, *Sol. Phys.*, 289, 2733
- Díaz, A. J., Soler, R., & Ballester, J. L. 2012, *ApJ*, 754, 41
- Ershkovich, A. I. 1980, *Space Sci. Rev.*, 25, 3
- Farrugia, C. J., Gratton, F. T., Bender, L., et al. 1998, *J. Geophys. Res.*, 103, 6703
- Foullon, C., Verwichte, E., Nakariakov, V. M., Nykyri, K., & Farrugia, C. J. 2011, *ApJ*, 729, L8
- Guglielmi, A. V., Potapov, A. S., & Klain, B. I. 2010, *Geomagnetism and Aeronomy*, 50, 958
- Hasegawa, H., Fujimoto, M., Phan, T.-D., et al. 2004, *Nature*, 430, 755
- Hester, J. J., Stone, J. M., Scowen, P. A., et al. 1996, *ApJ*, 456, 225
- Hillier, A. 2018, *Reviews of Modern Plasma Physics*, 2, 1
- Hillier, A. S. 2016, *MNRAS*, 462, 2256
- Hong, J., Jiang, Y., Zheng, R., et al. 2011, *ApJ*, 738, L20

- Innes, D. E., Cameron, R. H., Fletcher, L., Inhester, B., & Solanki, S. K. 2012, *A&A*, 540, L10
- Isobe, H., Miyagoshi, T., Shibata, K., & Yokoyama, T. 2005, *Nature*, 434, 478
- Kaiser, M. L., Kucera, T. A., Davila, J. M., et al. 2008, *Space Sci. Rev.*, 136, 5
- Kosugi, T., Matsuzaki, K., Sakao, T., et al. 2007, *Sol. Phys.*, 243, 3
- Kuridze, D., Zaqarashvili, T. V., Henriques, V., et al. 2016, *ApJ*, 830, 133
- Lemen, J. R., Title, A. M., Akin, D. J., et al. 2012, *Sol. Phys.*, 275, 17
- Li, X., Yang, S., Chen, H., Li, T., & Zhang, J. 2015, *ApJ*, 814, L13
- Li, X., Zhang, J., Yang, S., Hou, Y., & Erdélyi, R. 2018, *Scientific Reports*, 8, 8136
- Liberatore, S., Jaouen, S., Tabakhoff, E., & Canaud, B. 2009, *Physics of Plasmas*, 16, 044502
- Masters, A., Achilleos, N., Kivelson, M. G., et al. 2010, *Journal of Geophysical Research (Space Physics)*, 115, A07225
- Nisticò, G., Bothmer, V., Patsourakos, S., & Zimbardo, G. 2009, *Sol. Phys.*, 259, 87
- Ofman, L., & Thompson, B. J. 2011, *ApJ*, 734, L11
- Pesnell, W. D., Thompson, B. J., & Chamberlin, P. C. 2012, *Sol. Phys.*, 275, 3
- Pucci, S., Poletto, G., Sterling, A. C., & Romoli, M. 2013, *ApJ*, 776, 16
- Raouafi, N. E., Patsourakos, S., Pariat, E., et al. 2016, *Space Sci. Rev.*, 201, 1
- Rothschild, K., Pecker, J.-C., & Roberts, W. O. 1955, *ApJ*, 121, 224
- Ruderman, M. S., Verwichte, E., Erdélyi, R., & Goossens, M. 1996, *Journal of Plasma Physics*, 56, 285
- Ryutova, M., Berger, T., Frank, Z., Tarbell, T., & Title, A. 2010, *Sol. Phys.*, 267, 75
- Sakurai, T. 1976, *PASJ*, 28, 177
- Savcheva, A., Cirtain, J., Deluca, E. E., et al. 2007, *PASJ*, 59, S771
- Scherrer, P. H., Schou, J., Bush, R. I., et al. 2012, *Sol. Phys.*, 275, 207
- Schou, J., Scherrer, P. H., Bush, R. I., et al. 2012, *Sol. Phys.*, 275, 229

- Sen, A. K. 1964, *Physics of Fluids*, 7, 1293
- Severny, A.B., Khokhlova, V.L. 1953, *Izv. Krym. Astrofiz. Obs.* 10, 9
- Sharp, D. H. 1984, *Physica D Nonlinear Phenomena*, 12, 3
- Shen, Y., Liu, Y., Su, J., & Ibrahim, A. 2011, *ApJ*, 735, L43
- Shibata, K., Nitta, N., Strong, K. T., et al. 1994, *ApJ*, 431, L51
- Shimojo, M., Hashimoto, S., Shibata, K., et al. 1996, *PASJ*, 48, 123
- Sterling, A. C., Moore, R. L., Falconer, D. A., & Adams, M. 2015, *Nature*, 523, 437
- Stone, J. M., & Gardiner, T. 2007, *ApJ*, 671, 1726
- Suess, S. T., Ko, Y.-K., von Steiger, R., & Moore, R. L. 2009, *Journal of Geophysical Research (Space Physics)*, 114, A04103
- Taylor, G. 1950, *Proceedings of the Royal Society of London Series A*, 201, 192
- Tian, H., DeLuca, E. E., Cranmer, S. R., et al. 2014, *Science*, 346, 1255711
- Wang, C.-Y., & Chevalier, R. A. 2001, *ApJ*, 549, 1119
- Yang, L.-H., Jiang, Y.-C., Yang, J.-Y., et al. 2011a, *Research in Astronomy and Astrophysics*, 11, 1229
- Yang, S., Zhang, J., Li, T., & Liu, Y. 2011b, *ApJ*, 732, L7
- Ye, W. H., Wang, L. F., Xue, C., Fan, Z. F., & He, X. T. 2011, *Physics of Plasmas*, 18, 022704
- Yokoyama, T., & Shibata, K. 1995, *Nature*, 375, 42
- Zaqarashvili, T. V., Zhelyazkov, I., & Ofman, L. 2015, *ApJ*, 813, 123
- Zhelyazkov, I., & Chandra, R. 2018, *MNRAS*, 478, 5505
- Zhelyazkov, I., Chandra, R., & Srivastava, A. K. 2016, *Ap&SS*, 361, 51
- Zhelyazkov, I., Zaqarashvili, T. V., Chandra, R., Srivastava, A. K., & Mishonov, T. 2015, *Advances in Space Research*, 56, 2727

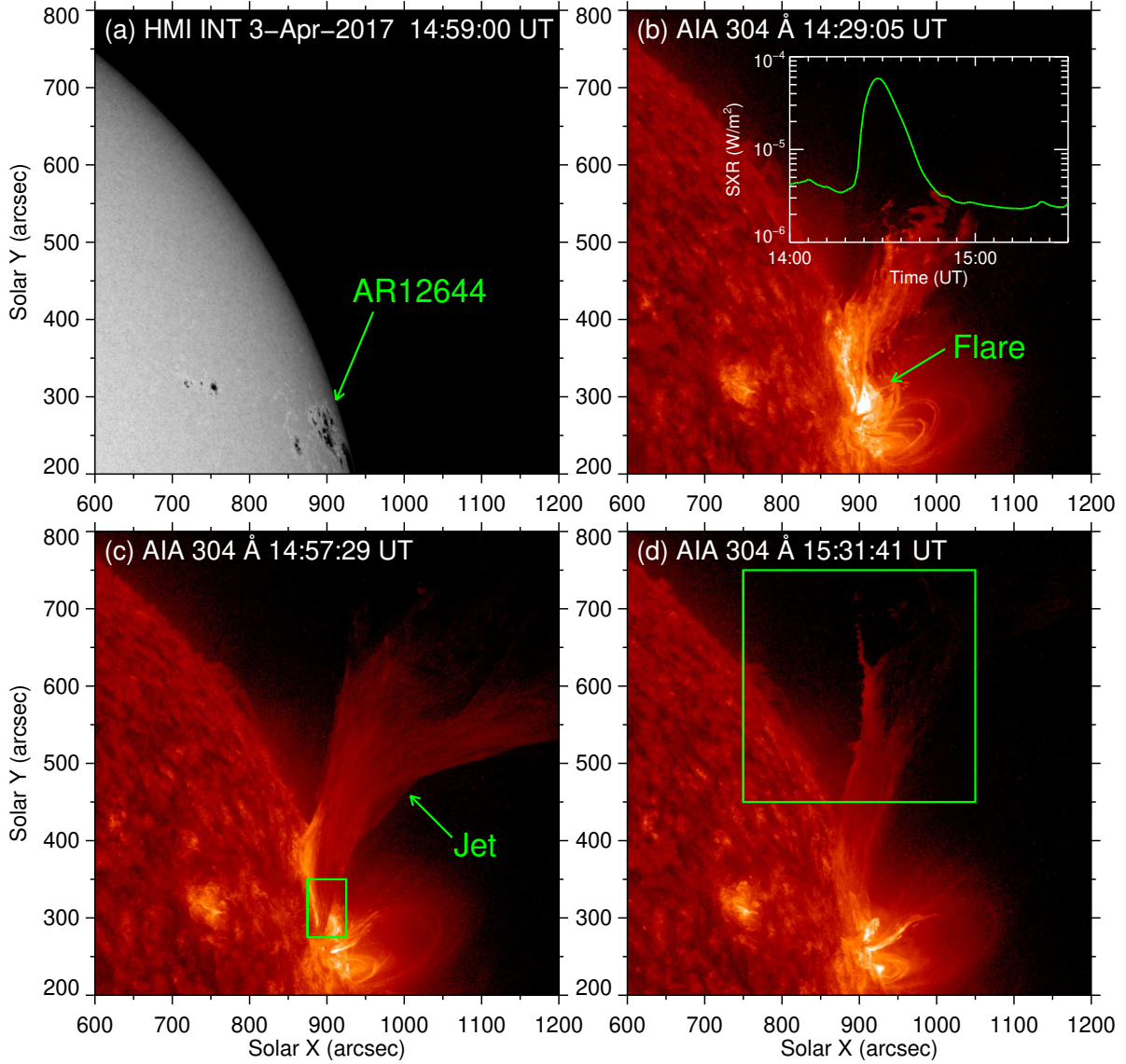


Fig. 1.— HMI continuum intensity (panel (a)) and AIA 304 Å images (panels (b)-(d)) displaying the overview of the jet on 2017 April 3. In panel (b), the green curve displays the variation of the *GOES* soft X-ray 1–8 Å flux. The green rectangle in panel (c) outlines the field-of-view (FOV) of Figure 2 and the green square in panel (d) outlines the FOV of Figure 3.

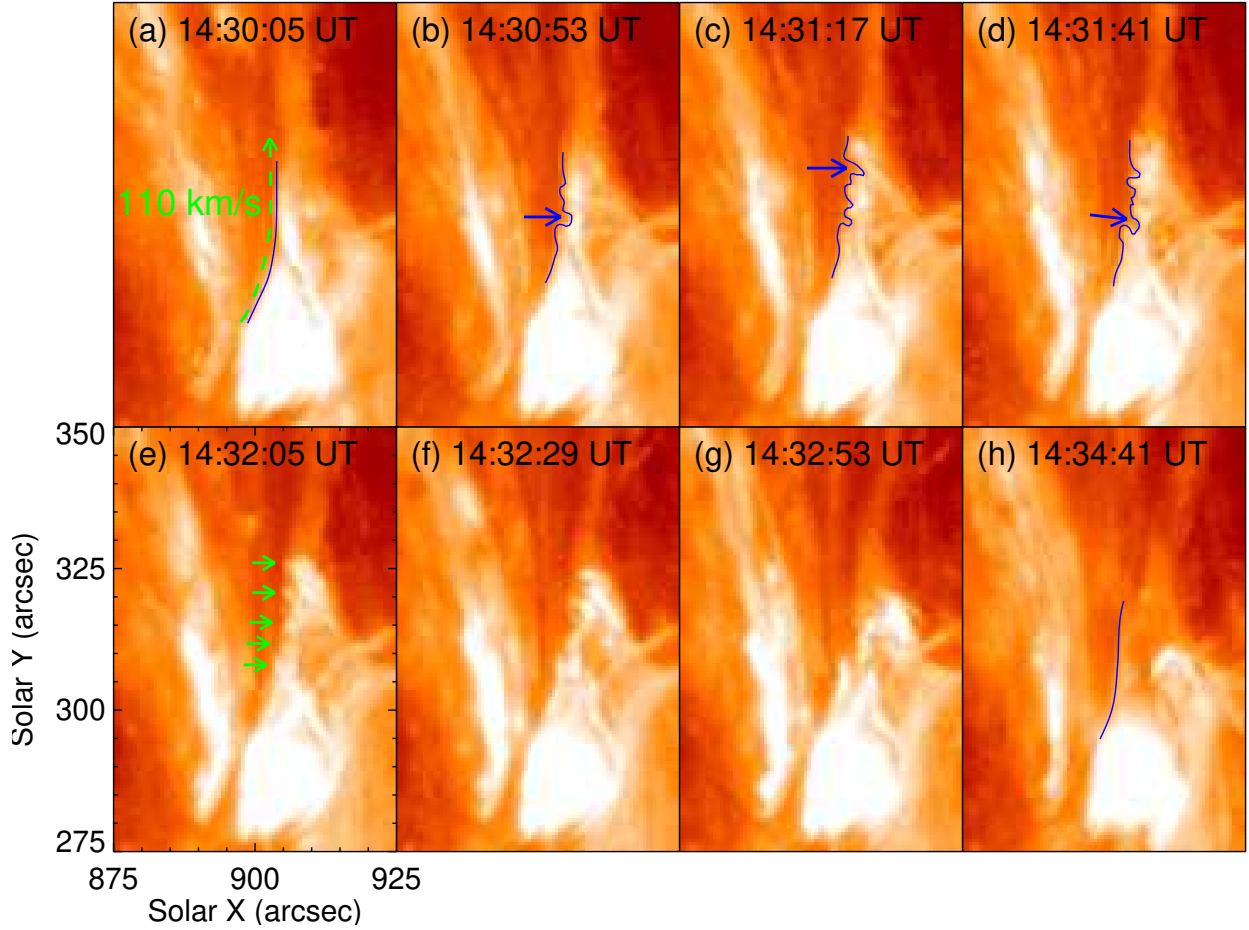


Fig. 2.— AIA 304 Å images showing the KHI in the upstream regime of the jet. The green dashed arrow in panel (a) displays the direction of the flow. In panels (a)-(d) and (h), the blue curves denote the left boundary of the jet. The green arrows in panel (e) point out five vortex-like structures caused by the KHI.

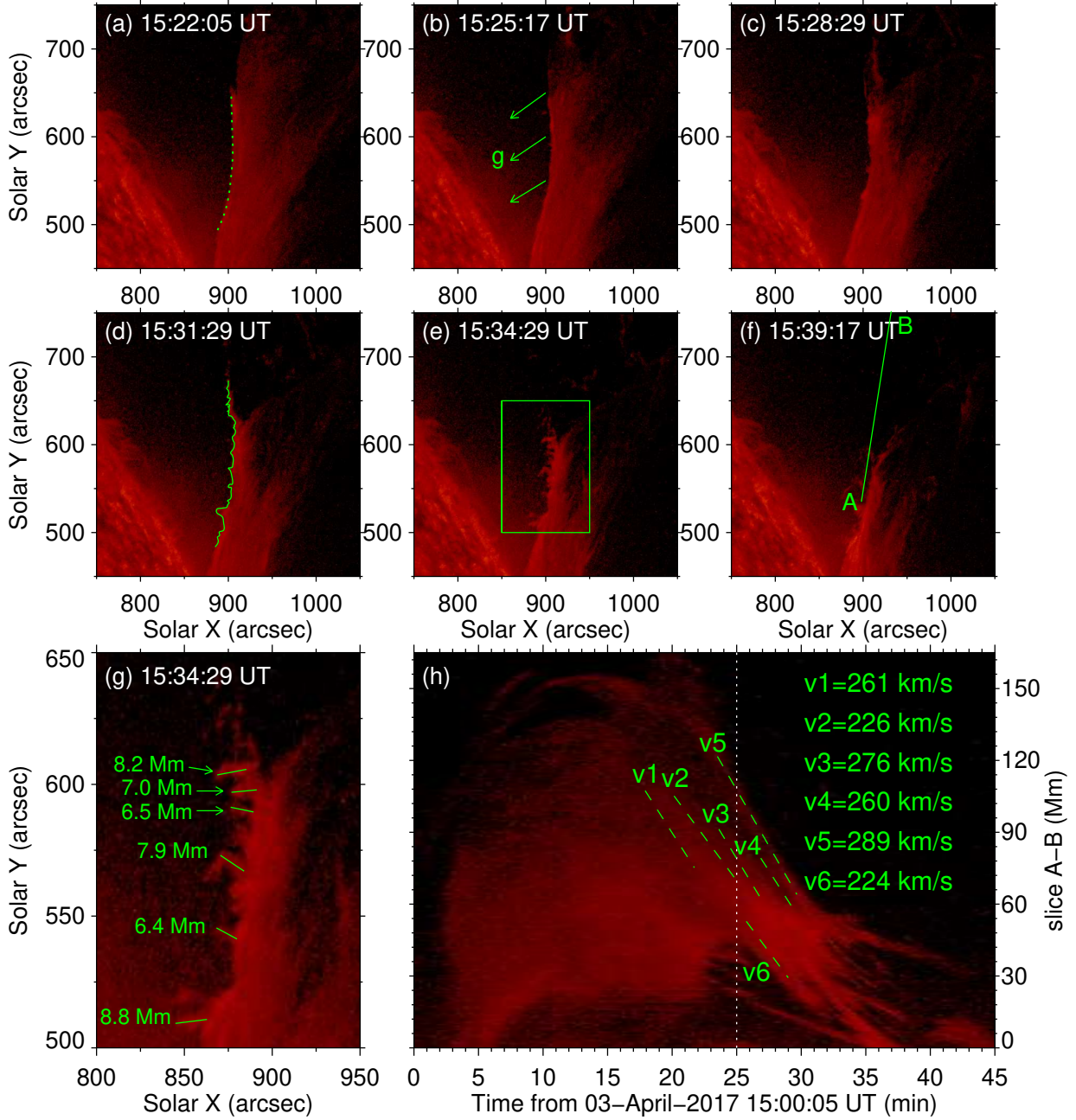


Fig. 3.— AIA 304 Å images (panels (a)-(f)) displaying the development of the vortex-like structures triggered by the falling material. The green curves in panels (a) and (d) denote the left boundary which changes from being smooth into a sawtooth pattern. The green arrows in panel (b) display the directions of gravity at the points where arrows start. Panel (g) shows the expanded view of the area outlined by the green rectangle in panel (e), and the distortion values (6.4 – 8.8 Mm) of six vortex-like structures are marked. Panel (h) displays the space-time plot along the slice “A-B” as marked in panel (f). The velocities of selected representative bright structures are displayed. The white dotted line indicates the occurrence time of the vortex-like structures. An animation (Movie1) of this figure is available.



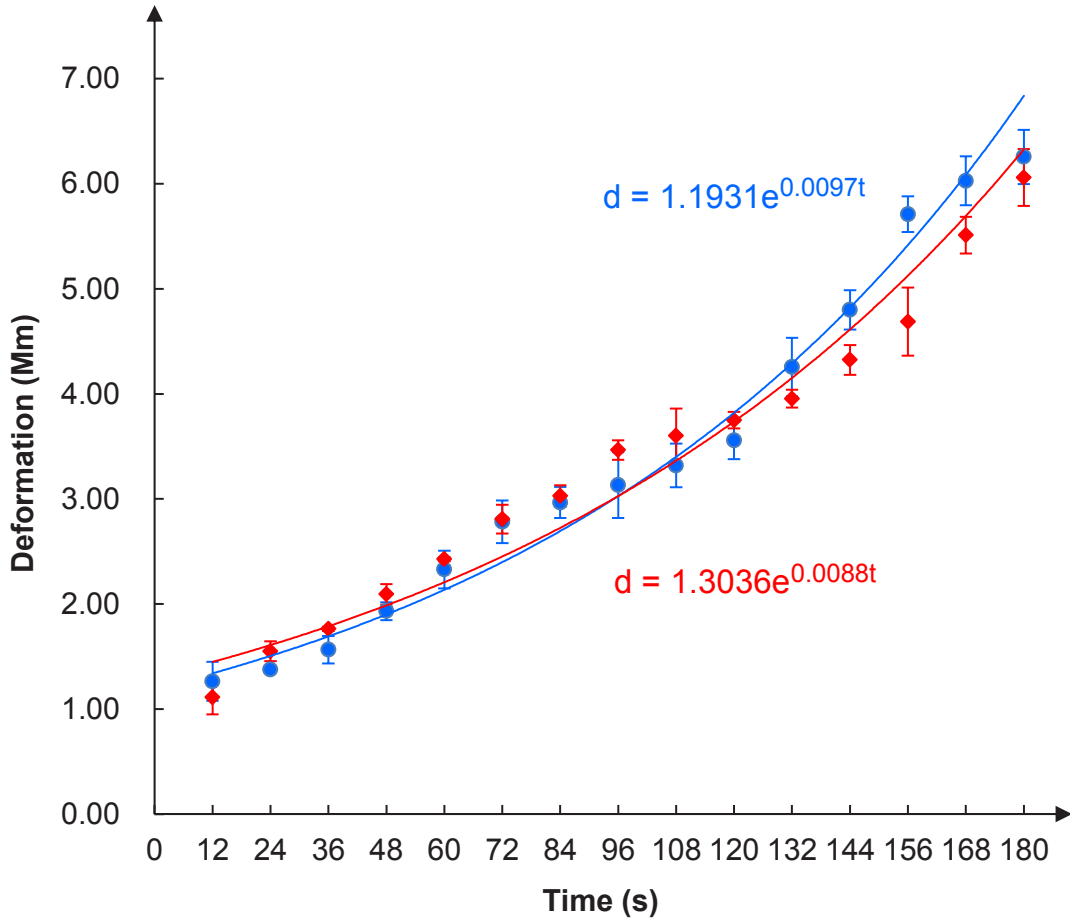


Fig. 4.— Growth rates of the vortex-like structures. We chose two structures in Figure 3(g) and measured their deformations over time for five times. The blue and red points plot the average values and the error bars indicate the standard deviations. The blue and red curves denote corresponding fitted curves, and the fitted equations are displayed beside.

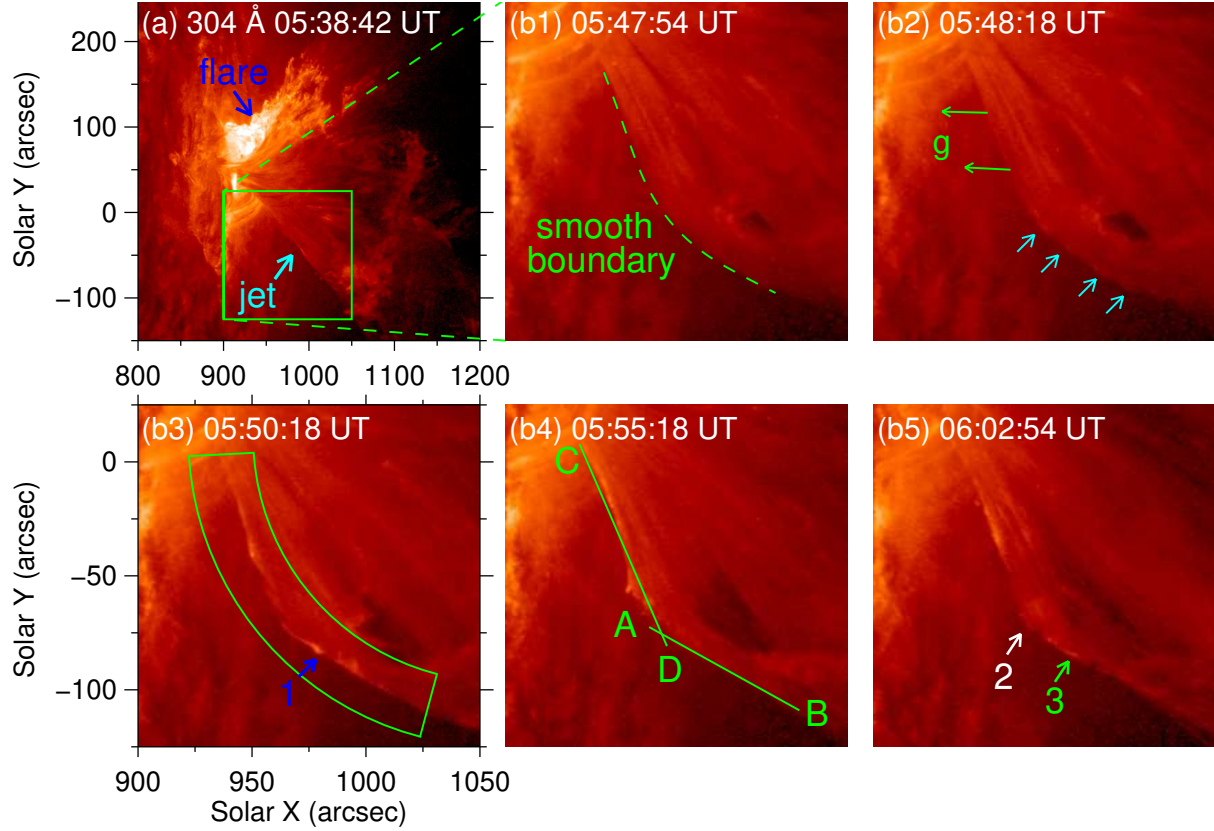


Fig. 5.— AIA 304 Å images displaying the vortex-like structures in the downstream regime of the jet on 2016 July 23. Panel (a): Appearances of the M5.5 class flare and the jet. Panels (b1)–(b5): Development of the vortex-like structures at the south boundary of the jet. The green arrows in panel (b2) display the directions of gravity at the points where arrows start. The cyan arrows in panel (b2) indicate several ripple structures. The green enclosed area in panel (b3) outlines the FOV of Figure 7. The numbered arrows in (b3) and (b5) indicate the structures which are displayed in Figure 7 with the same colors. In panel (b4), lines “A–B” and “C–D” display the cross-cut positions used to obtain the stack plots shown in Figure 6. An animation (Movie2) of this figure is available.

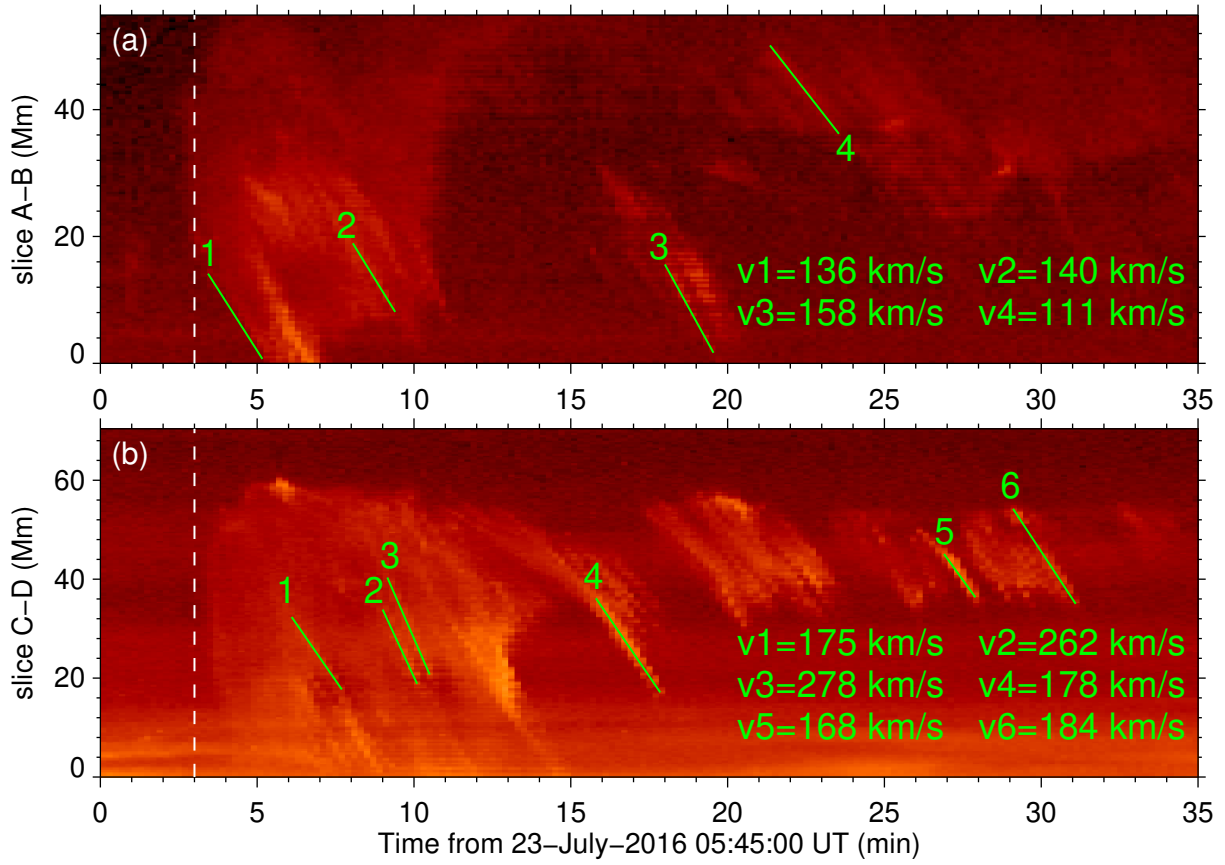


Fig. 6.— Temporal evolution at the positions of lines “A–B” and “C–D” in Figure 5(b4). The velocities of selected representative structures are displayed.

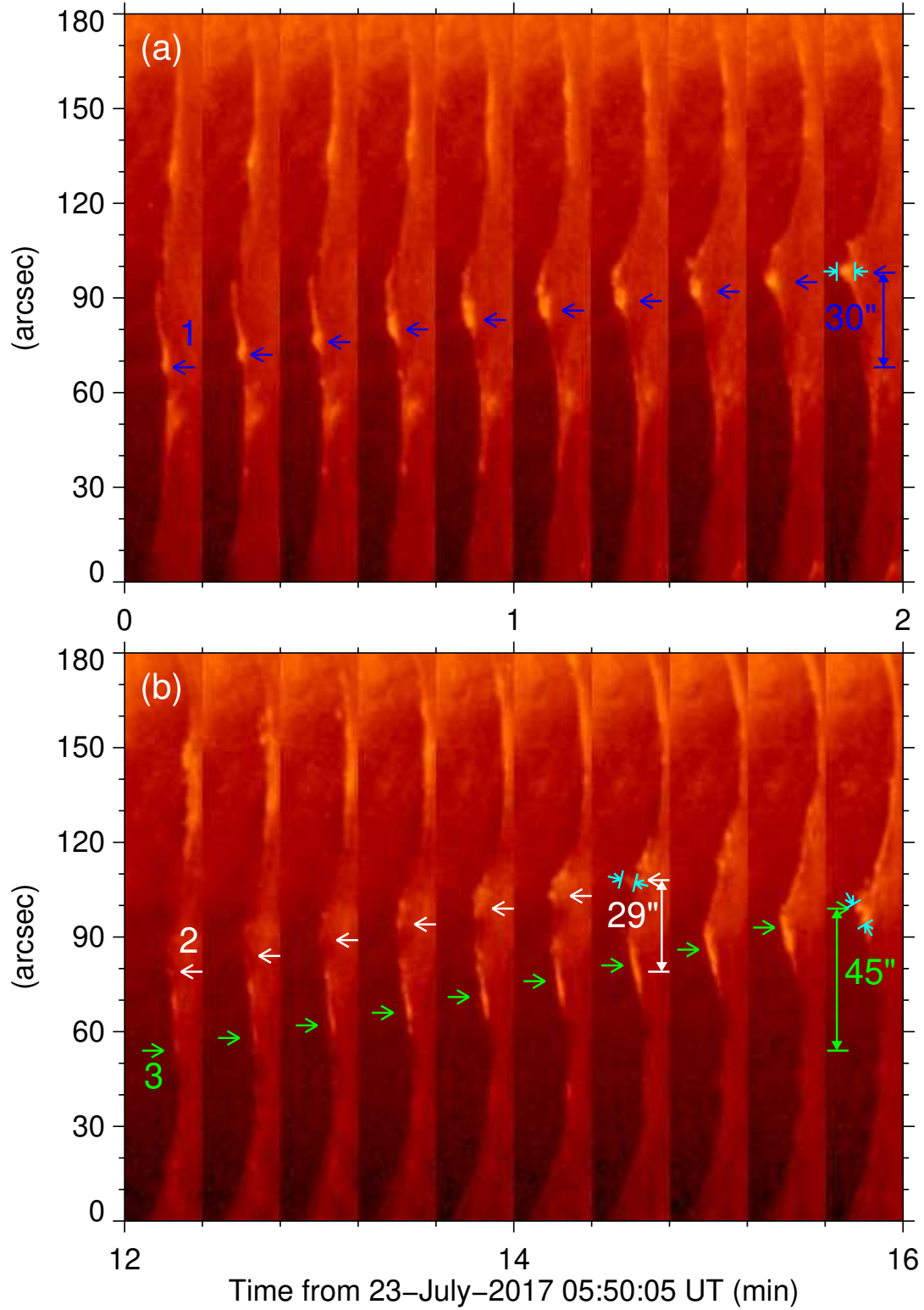


Fig. 7.— Development of south boundary of the jet. The arrows with same color denote the change of the location of the same vortex-like structure caused by the falling material. The diameter of each structure in the end is indicated by the cyan lines and arrows.